Three-port DC–DC converter based on quadratic boost converter for stand-alone PV/battery systems

Sajad Rostami[1], Vahid Abbasi[1] ✉, Nazilasadat Talebi[1], Tamas Kerekes[2]

[1]Department of Electrical Engineering, Faculty of Energy, Kermanshah University of Technology, Kermanshah, Iran
[2]Department of Energy Technology, Faculty of Engineering and Science, Aalborg University, Aalborg, Denmark
✉ E-mail: v_abbasi@kut.ac.ir

Abstract: In this study, a three-port DC–DC converter is proposed based on quadratic boost converter. The proposed converter contains paths to enable the flow of power from input source to load and battery. Furthermore, it makes a path available to energise the load by the battery. The proposed converter has a bidirectional path using two additional switches and two diodes. Power flows from the input source and the battery to the load in a single-stage resulting in higher efficiency. The proposed converter has three switches and two duty cycles defined. By adjusting the duty cycles, maximum input power and output voltage can be regulated based on the input source power and the battery condition. To control the proposed converter, three operation modes are defined. In order to design the control system, the proposed converter is analysed and the small-signal models are obtained. Using a decoupling network for the integrated small-signal models, separated closed-loop controllers are designed. Finally, a prototype for the proposed converter is prepared to validate feasibility and effectiveness of the proposed converter and the control method by experimental results.

1 Introduction

One of the drawbacks of renewable energy sources (RESs) is their intermittent energy availability. This can be minimised using energy storage (ES) in conjunction with them [1, 2]. Hence, two power electronic converters should be used for the combined system with which maximum input power of RES, output voltage and battery charging/discharging have to be controllable. Using individual converters for RES and ES leads to costly and inefficient system for power flow management. Three port converters (TPCs) integrate RES and ES and solve the problems of using separate converters. The advantages of TPCs include compact size, less components, cost-effective, better dynamic performance and less number of stages for controlling the system.

Based on sharing components such as switches, capacitors, inductors and diodes, new TPCs can be proposed. According to the strategy, different kinds of TPCs have been proposed and implemented in recent years. Selection of the proper topology depends on the application and converter characteristics. For instance, in integrating a solar source and a battery, a TPC has to provide two power flow paths consisting of a unidirectional path and a bidirectional path. The unidirectional path makes a connection between the solar resource and the load. The bidirectional path is necessary for battery charging and discharging. Classification of TPCs involve of three types: isolated, partly isolated and non-isolated converters.

Isolated TPCs contain a high frequency transformer that increases voltage gain and regulates voltage of the different ports to the desired values [3–5]. The components of the isolated TPCs are shared rarely between the power flow paths, which results in an increased number of components. Similar to the isolated TPCs, partly isolated topologies include a high frequency transformer for isolating the ports. The transformer increases power losses, lowers the efficiency and bigger size along with the increasing in voltage gain. Non-isolated TPCs can be proposed with compact size and less number of components due to sharing their components in power flow paths. Input source and battery are connected to load directly which limits application of non-isolated TPCs. According to the characteristics of non-isolated TPCs, they have been used as the best option for stand-alone applications that is the topic of this paper.

Most of the non-isolated TPCs have been proposed based on conventional converters. In [6], the structure of the TPC is combined from the buck–boost converter and it can be used in low voltage applications. Voltage gain of TPCs can be increased by a technique such as charge pump, which is integrated with boost converter, as presented in [7]. The proposed converter does not include a bidirectional power path that makes it inappropriate for stand-alone applications and integrating with a battery. Conventional converters such as buck, boost, buck–boost, Cuk and Sepic are reconfigured in [8] to present TPCs with different pros and cons. To equip the converters with bidirectional power flow path, a power switch and a diode are added to the structures and a battery is positioned between them [8]. The main drawback of the proposed structures is their low voltage gain. In addition, the battery may have undesirable charging and discharging modes during a cycle. Zhu *et al*. [9] proposes a TPC based on integration of a buck and a boost that has one additional inductor in its structure. However, the converter transfers high power density, its voltage gain is less than two. Thus, it cannot be used for most of the conventional applications. By integrating conventional converters, the other possible structures are proposed in [10]. The paper presents some combinations such as boost–Sepic, boost–boost, boost–buck, boost–Cuk and boost–Zeta for dual input and dual output configurations. There are more examples for structures based on the conventional converters [11–15] that have close characteristics to the discussed ones.

To increase the voltage gain, coupled-inductors can also be used in converters such as the ones presented in [13, 16, 17] that have been introduced as high step-up TPCs. The coupled inductors impose leakage inductance to the converter and increase conduction loss. In [13], the proposed converter is derived from [9] by adding two coupled inductors, one switch and four diodes. Due to the increased number of the components, soft switching method is applied in the converter to reduce switching losses [13]. Chen *et al*. [16] present a structure with two coupled inductors and five switches, which increases power loss and complicates control. The three-port converter in [17] has a balanced structure with three switches and one coupled inductor. Thus, it has an acceptable structure with less drawbacks.

This study proposes a non-isolated three-port converter composed of a quadratic boost DC–DC converter with a
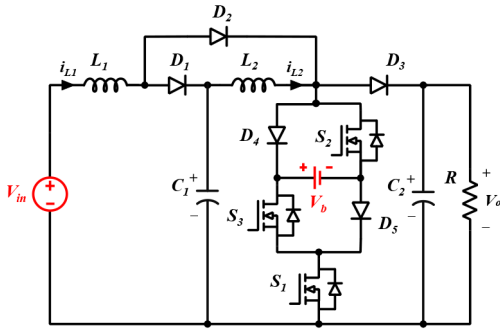
Fig. 1 *Structure of the proposed converter*

bidirectional path. Quadratic boost converter has continues input current and its voltage gain is equal to the boost converter voltage gain to the power of two. In comparison to the used conventional converters in the previous studies, the quadratic boost has higher voltage gain that makes it a good candidate. The bidirectional path consists of two diodes and three switches, out of which one is the converter power switch. The integration of the quadratic boost converter and the proposed bidirectional path can be introduced as a compact size TPC converter with appropriate characteristics. The converter is a single stage TPC with that battery charging/ discharging and supplying load power is possible in a cycle [18]. The input power and output voltage of the converter are controlled with two duty cycles. The duty cycles are decoupled to reduce complexity of the control.

This paper consists of different sections to study and analyse the converter. The proposed converter structure, its main equations for the operation modes and comparison with the other converters are described in Section 2 and Section 3. Section 4 describes dynamic modelling and control system of the converter. Design of the components are explained in Section 5. Section 6 includes experimental verifications and Section 7 concludes the proposed TPC.

2 Converter structure and operation modes

Fig. 1 presents structure of the proposed TPC based on quadratic boost converter. The converter is made up of one input source with battery to be used as a stand-alone system. Using the power switches (S_1, S_2 and S_3) and connected diodes to them (D_4 and D_5), the bidirectional path is provided. According to the structure, most of the components are common in different operation modes. Depending on the switching strategy, the path provides a bidirectional path or a unidirectional path to flow power between input source, battery and load. The used switching strategy enables the converter to control input power and output voltage with two independent duty cycles.

The input power of a renewable source (V_{in}) and the utilisation state of the battery determine the stand-alone TPCs operation mode. In general, a stand-alone converter has three operation modes, which are implemented by the two duty cycles. For the proposed converter, the duty cycles are decoupled to control input power and output voltage independently. One of the duty cycles is related to battery charging/discharging modes (d_2). Furthermore, the components are assumed ideal and the analysis is done for continuous conduction mode.

A DC source with constant voltage and a lead-acid battery are assumed as the PV source and the storage port, which interact to supply the load. The converter operation modes depend on the input power and the battery condition. When the maximum input power is equal to the load power, there is no need to use the battery for additional power and there is no additional power to charge the battery. This situation is introduced as the first operation mode in which the converter operates such as a quadratic boost converter. The second operation mode is set for high input power condition when the maximum input power is higher than output power. The input source supplies the load and charges the battery. The battery provides lack of power when the output power is higher than the

produced power in the input port. This situation is determined as the third operation mode.

2.1 First operation mode

In this operation mode, the converter operates as a quadratic converter and its control system is simple. The first operation mode has two switching states as Figs. 2a and b. Furthermore, the key waveforms of S_1, S_2, inductors current variation, and battery current variation are visible in Fig. 3a.

Switching state 1 ($0 < t < t_1$): at $t = 0$, the PWM signals turn on S_1 and S_2 that provide power flow paths to charge L_1 and L_2 by V_{in} and C_1, respectively. Voltage across L_1 and L_2 are equal to V_{in} and V_{C1}, respectively. With operating the switches and conducting D_2 and D_5, the state contains three loops as shown in Fig. 2a.

Switching state 2 ($t_1 < t < t_2$): At $t = t_1$, the switches are turned off. In this state, D_1 and D_3 are conducting and the other diodes are blocking. According to the drawn current path in Fig. 2b, inductors L_1 and L_2 are discharged into the load and voltage across them are equal to $V_{in} - V_{C1}$ and $V_{C1} - V_o$, respectively.

Using voltage-second balance theory, the following equations and voltage gain of the first mode operation can be concluded.

$$d_1 V_{in} - (1 - d_1)(V_{in} - V_{C1}) = 0 \qquad (1)$$

$$V_{C1} = \frac{V_{in}}{(1 - d_1)} \qquad (2)$$

$$d_1 V_{C1} - (1 - d_1)(V_{C1} - V_o) = 0 \qquad (3)$$

$$V_o = \frac{V_{C1}}{(1 - d_1)} \qquad (4)$$

where d_1 is duty cycle of S_1 and S_2 in the first switching state. Substituting (1) into (2), voltage gain of the converter in the first operation mode is as below

$$\frac{V_o}{V_{in}} = \frac{1}{(1 - d_1)^2} \qquad (5)$$

The mode has one duty cycle and it is utilised to regulate the output voltage on the reference value.

2.2 Second operation mode

In this operation mode, the input source supplies the load and charges the battery. The unidirectional and the bidirectional paths are utilised with four switching states as shown in Figs. 2a–c (the switching states 2 and 4 are similar which are shown by Fig. 2b). The converter operates with two duty cycles in the second operation mode. The power of the input source and output voltage can be regulated using the duty cycles. Furthermore, the key waveforms of the switches, inductors current variation and battery current variation are shown in Fig. 3b.

Switching state 1 ($0 < t < t_1$): the operation is similar to the first state of the first operation mode (Fig. 2a).

Switching state 2 ($t_1 < t < t_2$): the operation is similar to the second state of the first operation mode (Fig. 2b).

Switching state 3 ($t_2 < t < t_3$): at $t = t_2$, switch S_1 is turned on by a PWM signal and the inductors are charged by the input source and capacitor C_1 (Fig. 2c). Voltage across L_1 and L_2 are equal to $V_{in} - V_b$ and $V_{C1} - V_b$, respectively. The diodes D_4, D_5 and D_2 are conducting, which completes the inductors charging paths. In this state, the battery is charged by the input source and C_1. There are two loops to charge the battery and duty cycle of the state is equal to d_2.

Switching state 4 ($t_3 < t < T$): The operation in this state is similar to the second state (Fig. 2b).

Using voltage-second balance theory, the following equations and voltage gain of the second operation mode can be concluded.

$$L_1 : d_1 V_{in} - d_2(V_{in} - V_b) + (1 - (d_1 + d_2))(V_{in} - V_{C1}) = 0 \quad (6)$$

$$V_{C1} = \frac{V_{in} - d_2 V_b}{(1 - (d_1 + d_2))} \quad (7)$$

$$L_2 : d_1 V_{C1} + d_2(V_{C1} - V_b) + (1 - (d_1 + d_2))(V_{C1} - V_o) = 0 \quad (8)$$

$$V_o = \frac{V_{C1} - d_2 V_b}{(1 - (d_1 + d_2))} \quad (9)$$

Substituting (7) into (9), output voltage of the converter in the second operation mode is as below

$$V_o = \frac{V_{in} + V_b(d_2^2 - 2d_2 + d_1 d_2)}{(1 - (d_1 + d_2))^2} \quad (10)$$

when the battery is charging, the current and power can be obtained by the following equations.

$$i_b = -(I_{L1} + I_{L2}) \quad (11)$$

During the charging state, the inductors current is equal to

$$I_{L1} = \frac{I_o}{(1 - d_2)^2} \quad (12)$$

$$I_{L2} = \frac{I_o}{(1 - d_2)} \quad (13)$$

Substituting (12) and (13) into (11), the battery current, the battery average current and the battery power are

$$i_b = -\frac{I_o(2 - d_2)}{(1 - d_2)^2} \quad (14)$$

$$i_{b(ave)} = -\frac{I_o(2 - d_2)d_2}{(1 - d_2)^2} \quad (15)$$

$$P_b = V_b i_{b(ave)} = V_b \frac{I_o(2 - d_2)d_2}{(1 - d_2)^2} \quad (16)$$

2.3 Third operation mode

In this operation mode, the input source and the battery supply the load power when the input power is lower than the load power. The unidirectional and the bidirectional paths are utilised with four switching states as shown in Figs. 2a, b and d. The converter is a single stage and it operates with two duty cycles. Using the duty cycles, the input source power and output voltage should be controlled. Furthermore, the key waveforms of the switches, inductors current variation, and battery current variation are visible in Fig. 3c.

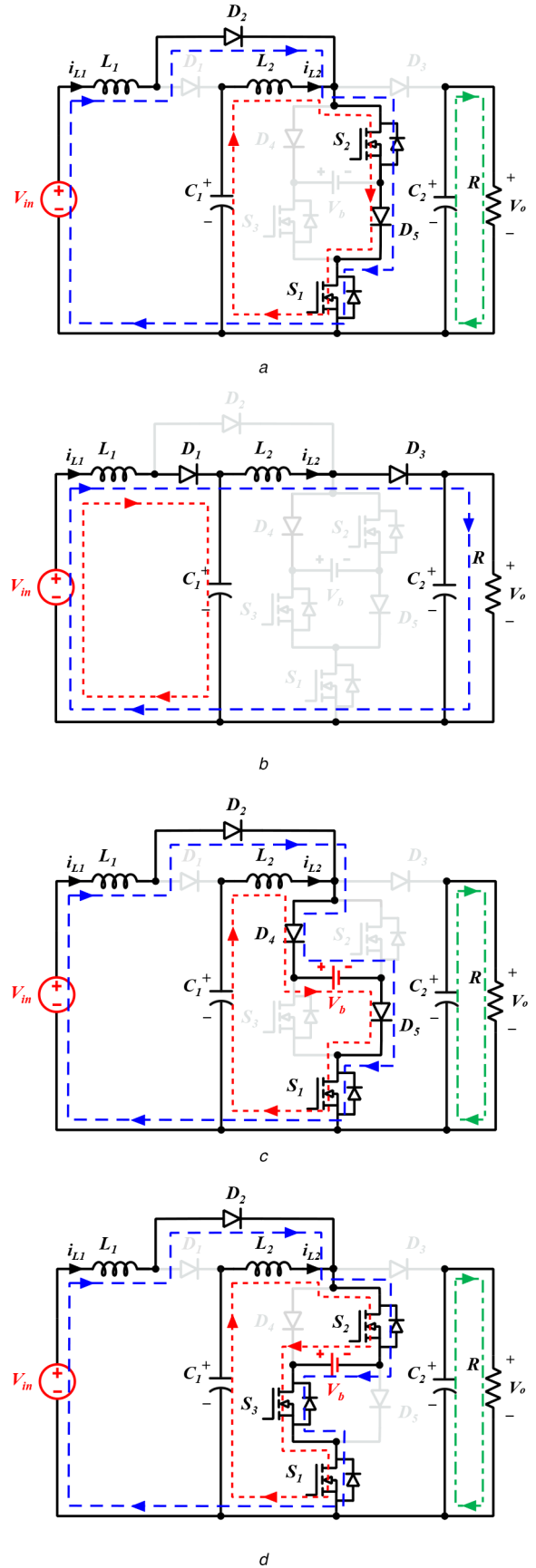*Switching state 1 (0 < t < t₁)*: the operation is similar to the first state of the first operation mode (Fig. 2a).

Switching state 2 (t₁ < t < t₂): the operation is similar to the second state of the first operation mode (Fig. 2b).

Switching state 3 (t₂ < t < t₃): at $t = t_2$, switches S_1, S_2 and S_3 are turned on by PWM signals and the inductors are charged by the input source, the battery and capacitor C_1 (Fig. 2d). Voltage across L_1 and L_2 are equal to $V_{in} + V_b$ and $V_{C1} + V_b$, respectively. The diode D_2 is conducting that completes the L_1 charging path (the other diodes are blocking). In order to offset the lack of power, the battery is discharged. There are two loops to discharge the battery and duty cycle of the state is equal to d_2.

Switching state 4 (t₃ < t < T): the operation in this state is similar to the second state (Fig. 2b).

Using voltage-second balance theory, the following equations and voltage gain of the third operation mode can be concluded.

$$L_1 : d_1 V_{in} + d_2(V_{in} + V_b) + (1 - (d_1 + d_2))(V_{in} - V_{C1}) = 0 \quad (17)$$

Fig. 2 *Switching states for the operation modes*
(a) Switching state 1: $(0 < t < t_1)$,
(b) Switching states 2 and 4: $(t_1 < t < t_2)$ and $(t_3 < t < T)$,
(c) Switching state 3: $(t_2 < t < t_3)$ for the second operation mode,
(d) Switching state 3: $(t_2 < t < t_3)$ for the third operation mode

$$V_{C1} = \frac{V_{in} + d_2 V_b}{(1 - (d_1 + d_2))} \quad (18)$$

$$L_2 : d_1 V_{C1} + d_2 (V_{C1} + V_b) + (1 - (d_1 + d_2))(V_{C1} - V_o) = 0 \quad (19)$$

$$V_o = \frac{V_{C1} + d_2 V_b}{(1 - (d_1 + d_2))} \quad (20)$$

Substituting (18) into (20), output voltage of the converter in the third operation mode is as below

$$V_o = \frac{V_{in} + V_b(-d_2^2 + 2d_2 - d_1 d_2)}{(1 - (d_1 + d_2))^2} \quad (21)$$

When the battery is discharging, it's current can be obtained by the following equation

$$i_b = (I_{L1} + I_{L2}) \quad (22)$$

The battery current, average of the current and the battery power have equations as same as the second operation mode in opposite directions.

Output voltage curves of the proposed converter for different conditions are illustrated in Fig. 4. The curves are drown using (5), (10) and (21). The battery voltage and the input source voltage are assumed to be 12 and 25 V, respectively (similar to the values in the experiments). The results are shown with $d_1 = 0.37$ and $d_2 = 0.2$ in charging mode and $d_2 = 0.3$ in discharging mode, the voltage gain is equal to 6. The voltage gain is obtainable for the converter with conventional terms.

The high voltage gain of the proposed converter can be considered as an advantage over other TPCs based on conventional converters.

3 Comparison with the other converters

To confirm the proposed converter advantages, some of the important factors are compared with similar converters. The proposed converter is a non-isolated three-port converter. Thus, Table 1 contains non-isolated converters with structures close to the proposed one. The main comparison factors include number of components, voltage gain, continuous input current, containing bidirectional path and common ground, efficiency in nominal power for the operation modes and maximum efficiency.

PV panels have low nominal voltage that has to be increased appropriately for most of the applications. Thus, voltage gain is the main factor that is comparable by the equations in Table 1. Voltage gain of the proposed converter is higher than the converters in [9, 19, 21]. Furthermore, voltage gain of the proposed converter is higher than the converters in [20, 22] per high duty cycles (per $D > 0.5$ it is higher than [20] and per $D \geq 0.6$ it is higher than [22]). The converter in [7] boosts voltage with higher gain, but it does not contain bidirectional path to charge and discharge battery. Therefore, the converter in [7] cannot be utilised in PV/battery system that is topic of this paper. Number of the used components in the converters varies from 11 to 23. The proposed converter includes 12 components that shows its volume is suitable for being proposed as a three-port converter. In comparison to the converters in [9, 19, 20], the proposed converter has an additional component which is negligible due to its higher voltage gain.

DC–DC converters with common ground have more safety, less protection problems and reduced EMI. Furthermore, there is no additional d_V/d_t between input and output grounds. All the compared converters and the proposed one have a common ground between the load and input source. Thus, it contains the positive property similar to the others.

Low number of the used components in the proposed converter causes reduction of power losses and its efficiency per different operation modes is high. The proposed converter efficiency is
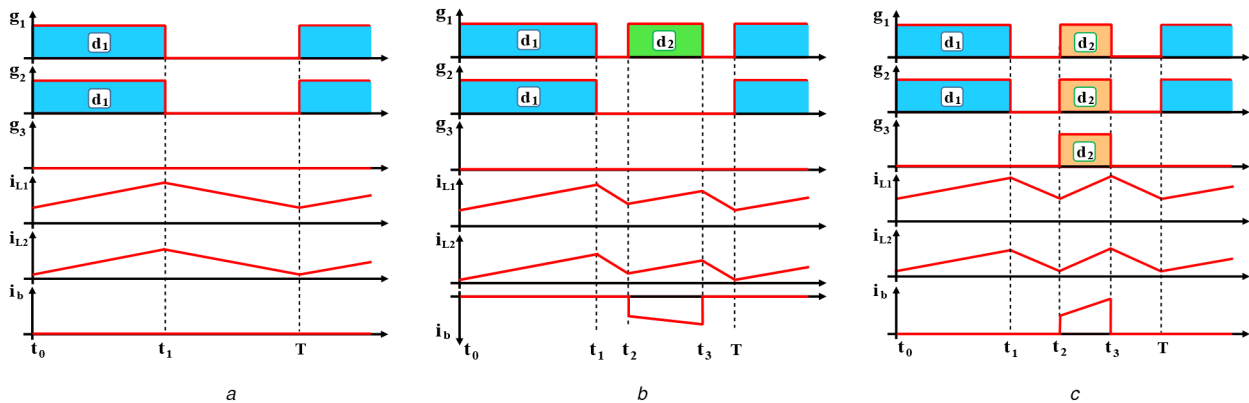
Fig. 3 *State waveform of the proposed converter in*
(a) First operation mode,
(b) Second operation mode,
(c) Third operation mode
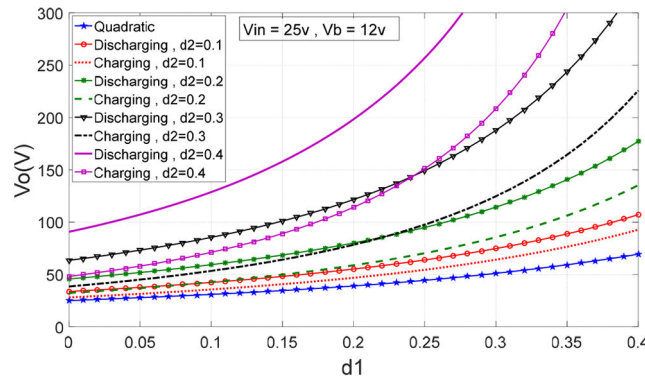
Fig. 4 *Output voltage of the proposed converter for different operation conditions – quadratic: first operation mode, charging: second operation mode and discharging: third operation mode*

Table 1 Comparison of the proposed converter with the other converters

Structures	[19]	[7]	[9]	[20]	[21]	[22]	Proposed converter
number of switches	4	2	3	4	6	6	3
number of diodes	4	5	1	4	4	2	5
number of inductors	2	2	3	1	3	4	2
number of capacitors	1	5	4	2	10	4	2
number of the used components	11	14	11	11	23	16	12
voltage gain	$\frac{1}{(1-d)}$	$\frac{5}{(1-d)}$	$\frac{1}{(1-d)}$	$\frac{2}{(1-d)}$	$\frac{1}{(1-d)}$	$\frac{(3-d)}{(1-d)}$	$\frac{1}{(1-d)^2}$
continuous input current	yes	yes	yes	no	no	yes	yes
bidirectional path	yes	no	yes	yes	yes	yes	yes
common ground	yes	yes	yes	yes	yes	yes	yes
conversion efficiency (at nominal power)	80%	91.4%	93.5%	88%–90%	95%	87%–93%	91%–93%
peak efficiency	80%	96%	96%	90%	95%	93%	96%

higher than the converters in [19, 20, 22]. Furthermore, the highest efficiency value of the proposed converter is close to the converters in [7, 9, 21].

Continuously of input current is a quality factor for some applications. In comparison to the converters in [20, 21], the proposed converter has this advantage.

As the main results of the comparisons, the proposed converter includes positive points from view of the main quality factors. The positive points can be considered by its higher voltage gain, acceptable number of the used components, continuously of input current, existence of a bidirectional path, existence of a common ground and high efficiency of its performance. It is worthy to say, none of the compared converters have the advantages at the same time and each of them has one or two drawbacks in comparison to the proposed converter. For more clarification, the main drawbacks of the converters in comparison to the proposed one are underlined in Table 1.

Thus, the proposed converter can be presented as a high voltage gain converter with noticeable positive points for PV/battery systems.

4 Dynamic modelling and control system

As noticed in the previous section, the proposed converter operates in three operation modes, which need to have proper control strategies. The first operation mode includes one duty cycle, while two duty cycles are utilised in the second and third operation modes. There are interactions between the control variables and control loops that make controlling the system difficult. To overcome the problem, using decoupling network seems proper that separates the control loops. Thus, the control system can be designed to regulate the variables individually with acceptable speed. Investigating transient operation and stability of the proposed converter requires extracting small signal model for the operation modes [19, 23–25]. Furthermore, review of the control loops is easy by the small signal models. First, state–space average models of the converter should be defined for the operation modes as follows [19, 23–25]. The converter includes four state variables (i_{L1}, i_{L2}, v_{C1} and v_{C2}) and the average models are investigated for them. Eventually, i_{L1} and v_{C2} are utilised to control input power and output voltage respectively ($i_{L1} = i_{in}$ and $v_{C2} = V_o$).

- *First operation mode*: the first operation mode has one duty cycle (d_1) that is the base of the state–space averaged model. Using the equivalent circuits of the switching states in Figs. 2a and b, the averaged model is

$$L_1 \frac{di_{L1}}{dt} = v_{in} - v_{C1}(d_1 - 1)$$

$$L_2 \frac{di_{L2}}{dt} = v_{C1} + v_{C2}(d_1 - 1)$$

$$C_1 \frac{dv_{C1}}{dt} = i_{L1}(1 - d_1) - i_{L2}$$

$$C_2 \frac{dv_{C2}}{dt} = i_{L2}(1 - d_1) - \frac{v_{C2}}{R}$$

$$(23)$$

- *Second operation mode*: the second operation mode contains two duty cycles (d_1 and d_2) which appear in the averaged model. Using the equivalent circuits of the switching states in Fig. 2a–c, the averaged model is

$$L_1 \frac{di_{L1}}{dt} = v_{in} - v_B d_1 + v_{C1}(d_1 + d_2 - 1)$$

$$L_2 \frac{di_{L2}}{dt} = v_{C1} - v_B d_1 + v_{C2}(d_1 + d_2 - 1)$$

$$C_1 \frac{dv_{C1}}{dt} = i_{L1}(1 - d_1 - d_2) - i_{L2}$$

$$C_2 \frac{dv_{C2}}{dt} = i_{L2}(1 - d_1 - d_2) - \frac{v_{C2}}{R}$$

$$(24)$$

- *Third operation mode*: similar to the second operation mode, the averaged model are formed by the two duty cycles (d_1 and d_2). Using the equivalent circuits of the switching states in Figs. 2a, b and d, the averaged model is:

$$L_1 \frac{di_{L1}}{dt} = v_{in} + v_B d_1 + v_{C1}(d_1 + d_2 - 1)$$

$$L_2 \frac{di_{L2}}{dt} = v_{C1} + v_B d_1 + v_{C2}(d_1 + d_2 - 1)$$

$$C_1 \frac{dv_{C1}}{dt} = i_{L1}(1 - d_1 - d_2) - i_{L2}$$

$$C_2 \frac{dv_{C2}}{dt} = i_{L2}(1 - d_1 - d_2) - \frac{v_{C2}}{R}$$

$$(25)$$

Small signal models are obtainable by changing the variables in the state–space averaged models [19, 23–25]. According to perturbation theory, all the variable parameters as input voltage (V_{in}), output voltage (V_o), the state variables (x) and duty cycles (d) have to be considered with DC values and perturbations as [19, 23–25]

$$u = \bar{U} + \tilde{u}, \quad d = \bar{D} + \tilde{d}, \quad x = \bar{X} + \tilde{x}, \quad v = \bar{V} + \tilde{v} \quad (26)$$

where ($\bar{U}$, $\bar{D}$, $\bar{X}$, $\bar{V}$) and ($\tilde{u}$, $\tilde{d}$, $\tilde{x}$, $\tilde{v}$) are DC values and perturbations of variable, respectively. Small signal models allow studying the effects of very small variations on the converter operation. Assumption of small perturbations as $\tilde{x} \ll \bar{X}$, $\tilde{u} \ll \bar{U}$, $\tilde{v} \ll \bar{V}$ and $\tilde{d} \ll \bar{D}$ makes the study possible. Substituting (26) into

the state–space averaged models ((23)–(25)), gives small signal models. Since the second-order terms of the perturbations ($\tilde{x} \cdot \tilde{x}$, $\tilde{d} \cdot \tilde{x}$ and …) have too small values, they can be eliminated from the equations. The small signal equations can be categorised in matrix forms with the following equation:

$$\dot{\tilde{x}} = A\tilde{x} + B\tilde{u}$$
$$\tilde{y} = C\tilde{x} + D\tilde{u} \tag{27}$$

where $\tilde{u}$, $\tilde{x}$, $\tilde{y}$ are control variables vector, state variable vector and output variable vector, respectively. In the following, small signal models of the operation modes are reformed using (23)–(25) and (27).

First mode:

$$A = \begin{bmatrix} 0 & 0 & 0 & \dfrac{d_1 - 1}{L_1} \\ 0 & 0 & \dfrac{d_1 - 1}{L_2} & \dfrac{1}{L_2} \\ 0 & \dfrac{1 - d_1}{C_2} & -\dfrac{1}{RC_2} & 0 \\ \dfrac{1 - d_1}{C_1} & -\dfrac{1}{C_1} & 0 & 0 \end{bmatrix}, \quad B = \begin{bmatrix} \bar{v}_{C1} \\ \bar{v}_{C2} \\ -\bar{i}_{L2} \\ -\bar{i}_{L1} \end{bmatrix}$$
(28)

$$\tilde{x} = \begin{bmatrix} \tilde{i}_{L1} \\ \tilde{i}_{L2} \\ \tilde{v}_{C2} \\ \tilde{v}_{C1} \end{bmatrix}, \quad \tilde{u} = \tilde{d}_1, \quad C = \begin{bmatrix} 0 & 0 & 0 & 0 \\ 0 & 0 & 0 & 0 \\ 0 & 0 & 1 & 0 \\ 0 & 0 & 0 & 0 \end{bmatrix}$$

Second mode:
   (see (29))
   Third mode:
   (see (30))

4.1 Decoupled control system

The two duty cycles of the second and third operation modes have interactions, which should be decoupled with decoupling-network method [19, 23–25]. In the first step, transfer function matrix of the small-signal models for each operation mode have to be formed as below

$$G = C(SI - A)^{-1}B + D \tag{31}$$

Number of control variables in the modes determines orders of the transfer function matrix. Thus, two G_{2-2} type matrixes consider transfer function of the second and third operation modes. Using G_{2-2} matrix, the output variables matrix in (27) has to be rewritten as follows [19, 23–25]:

$$\begin{bmatrix} y_1 \\ y_2 \end{bmatrix} = \begin{bmatrix} g_{11} & g_{12} \\ g_{21} & g_{22} \end{bmatrix} \begin{bmatrix} u_1 \\ u_2 \end{bmatrix} \tag{32}$$

where y_i, u_j and g_{ij} are ith input vector, jth output vector and transfer function between y_i and u_j, respectively. The decoupling-network method for 2 and 3 variables have been explained in several references such as [19, 25]. To shorten the discussion, the concluded equation of the method for two control variables system is used from [19, 25]. The cross-coupled two-loop control system can be decoupled into independent systems as shown in (33)

$$\frac{y_1}{u_1} = g_{11} - g_{12}\frac{g_{21}}{g_{22}}$$
$$\frac{y_2}{u_2} = -g_{12}\frac{g_{21}}{g_{11}} + g_{22} \tag{33}$$

Using (31)–(33) the two decoupled transfer functions for the system can be extracted, respectively. Resulting equations divide the control system to two independent single-input single-output systems. In order to design controllers for the decoupled loops, bode plot analysis is utilised, which specifies phase margin and

$$A = \begin{bmatrix} 0 & 0 & 0 & \dfrac{d_1 + d_2 - 1}{L_1} \\ 0 & 0 & \dfrac{d_1 + d_2 - 1}{L_2} & \dfrac{1}{L_2} \\ 0 & \dfrac{1 - d_1 - d_2}{C_2} & -\dfrac{1}{RC_2} & 0 \\ \dfrac{1 - d_1 - d_2}{C_1} & -\dfrac{1}{C_1} & 0 & 0 \end{bmatrix}, \quad B = \begin{bmatrix} \dfrac{\bar{v}_{C1} - \bar{v}_B}{L_1} & \dfrac{\bar{v}_{C1}}{L_1} \\ \dfrac{\bar{v}_{C2} - \bar{v}_B}{L_2} & \dfrac{\bar{v}_{C2}}{L_2} \\ -\dfrac{\bar{i}_{L2}}{C_2} & -\dfrac{\bar{i}_{L2}}{C_2} \\ -\dfrac{\bar{i}_{L1}}{C_1} & -\dfrac{\bar{i}_{L1}}{C_1} \end{bmatrix}$$
(29)

$$\tilde{x} = \begin{bmatrix} \tilde{i}_{L1} \\ \tilde{i}_{L2} \\ \tilde{v}_{C2} \\ \tilde{v}_{C1} \end{bmatrix}, \quad \tilde{u} = \begin{bmatrix} \tilde{d}_1 \\ \tilde{d}_2 \end{bmatrix}, \quad C = \begin{bmatrix} 1 & 0 & 0 & 0 \\ 0 & 0 & 0 & 0 \\ 0 & 0 & 1 & 0 \\ 0 & 0 & 0 & 0 \end{bmatrix}$$

$$A = \begin{bmatrix} 0 & 0 & 0 & \dfrac{d_1 + d_2 - 1}{L_1} \\ 0 & 0 & \dfrac{d_1 + d_2 - 1}{L_2} & \dfrac{1}{L_2} \\ 0 & \dfrac{1 - d_1 - d_2}{C_2} & -\dfrac{1}{RC_2} & 0 \\ \dfrac{1 - d_1 - d_2}{C_1} & -\dfrac{1}{C_1} & 0 & 0 \end{bmatrix}, \quad B = \begin{bmatrix} \dfrac{\bar{v}_{C1} + \bar{v}_B}{L_1} & \dfrac{\bar{v}_{C1}}{L_1} \\ \dfrac{\bar{v}_{C2} + \bar{v}_B}{L_2} & \dfrac{\bar{v}_{C2}}{L_2} \\ -\dfrac{\bar{i}_{L2}}{C_2} & -\dfrac{\bar{i}_{L2}}{C_2} \\ -\dfrac{\bar{i}_{L1}}{C_1} & -\dfrac{\bar{i}_{L1}}{C_1} \end{bmatrix}$$
(30)

$$\tilde{x} = \begin{bmatrix} \tilde{i}_{L1} \\ \tilde{i}_{L2} \\ \tilde{v}_{C2} \\ \tilde{v}_{C1} \end{bmatrix}, \quad \tilde{u} = \begin{bmatrix} \tilde{d}_1 \\ \tilde{d}_2 \end{bmatrix}, \quad C = \begin{bmatrix} 1 & 0 & 0 & 0 \\ 0 & 0 & 0 & 0 \\ 0 & 0 & 1 & 0 \\ 0 & 0 & 0 & 0 \end{bmatrix}$$

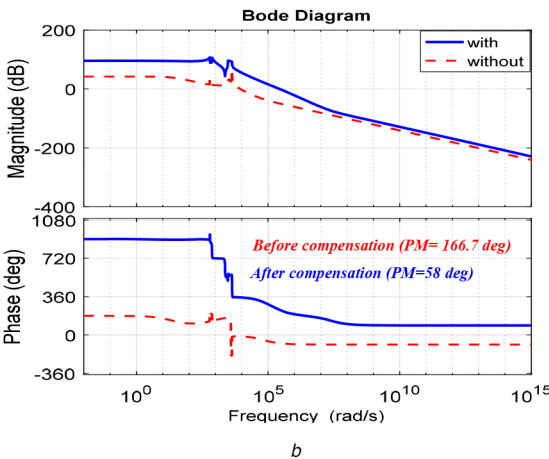**Table 2** Designed compensators for the operation modes

Operation mode	First	Second	Third
G_{vo}	$K = 100$	$K = 100$	$K = 300$
	$T = 0.00004$	$T = 0.00005$	$T = 0.000004101$
	$\alpha T = 0.000004$	$\alpha T = 0.0000055$	$\alpha T = 0.0000004101$
G_{iL}	—	$K = 0.01$	$K = 0.01$
	—	$T = 0.1$	$T = 0.01$
	—	$\alpha T = 0.001$	$\alpha T = 0.01$
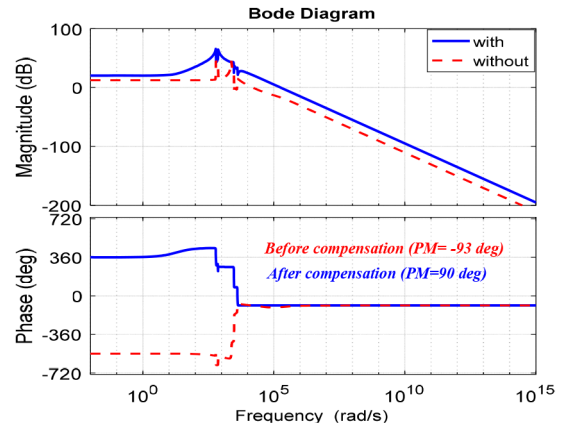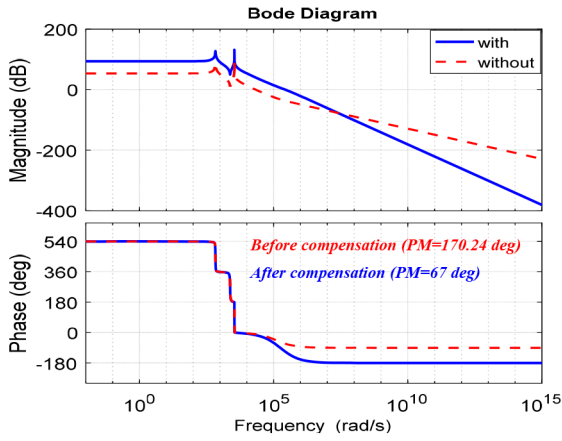
Fig. 5 *Bode diagrams of the first operation mode ($v_o(s)/d_1(s)$)*

a

b

Fig. 6 *Bode diagrams of the second operation mode*
(a) ($i_L(s)/d_1(s)$),
(b) ($v_o(s)/d_2(s)$)

a

b
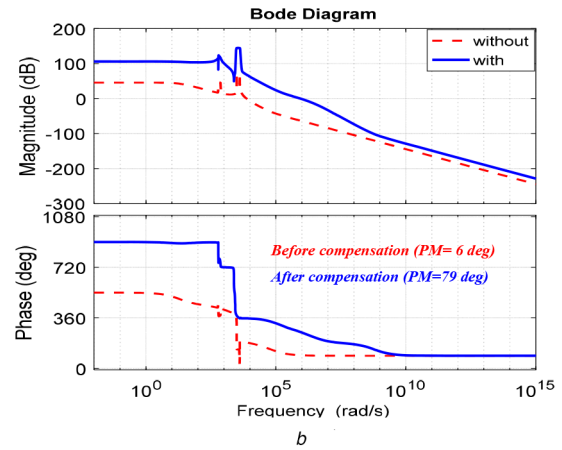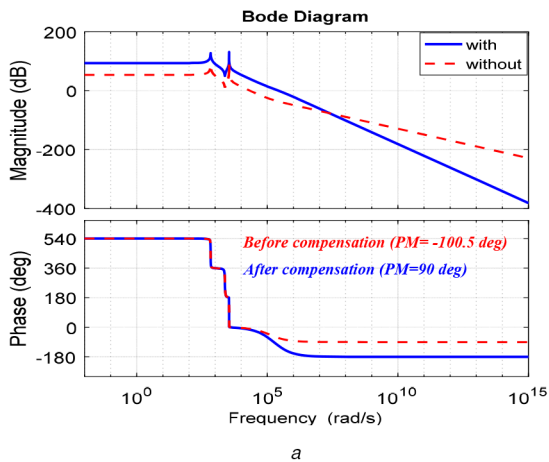
Fig. 7 *Bode diagrams of the third operation mode*
(a) ($i_L(s)/d_1(s)$),
(b) ($v_o(s)/d_2(s)$)

integration unit and a lead unit. The integration unit eliminates the steady state errors by increasing the system type. Furthermore, the regulation of the system with the form results a suitable phase margin and an increased cut off frequency due to the presence of lead unit in the compensator function. Based on the explained procedure, the compensators are designed and listed in Table 2, where G_{vo} and G_{iL} are designed compensators for the controller of output voltage and input power, respectively.

To investigate the effects of the compensators, bode plots of open-loops and closed loops are drawn in Figs. 5–7. The Figures show the bode diagrams of input current and output voltage functions for the three operation modes. The compensators are implemented to limit phase margins in the range of 55°–90°. According to the bode diagrams, slope of the diagrams in low frequencies are low and have been decreased by the integral units. Thus, the steady-state error of the controlled parameters tends to zero. The compensators are composed of an integration unit and lead/lag unit, which have to increase the overall cutoff frequency. The results in the bode plots illustrate increasing cutoff frequencies in the operation modes that enhances speed of the system responses. Therefore, the main goals consisting of stability, steady-state error equal to zero and higher speed of system response are available by the designed compensators.

gain margin of the decoupled systems. The compensators are set to achieve standards such as desired steady-state error, stability and phase margin in a specified range. For the compensators, a general form of them as $K(1 + Ts)/s(1 + \alpha Ts)$ is chosen, which contains an
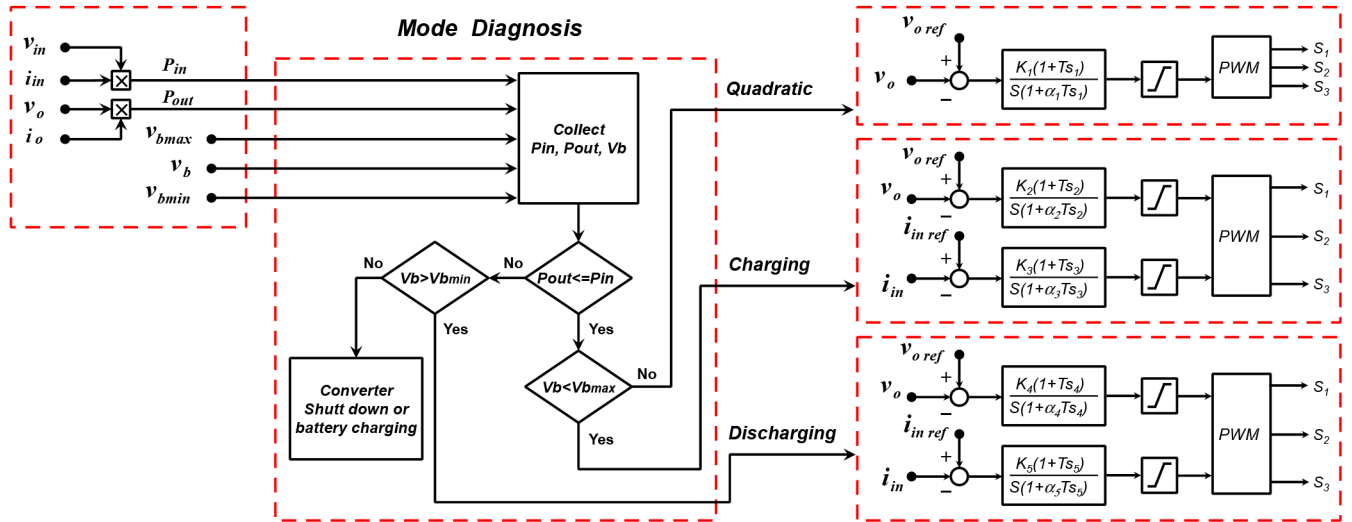
Fig. 8 *Control diagram for the operation modes of the proposed converter – the diagram includes feedbacks, power calculations, mode diagnosis unit and control of the modes*
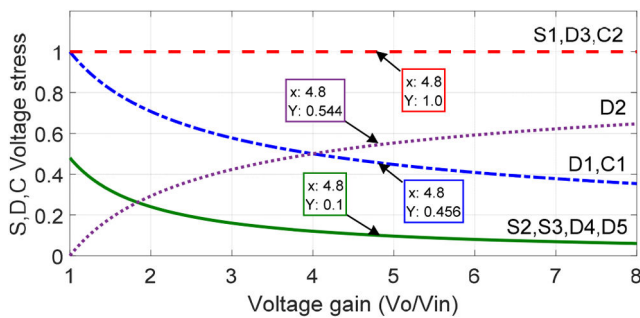
Fig. 9 *Normalised voltage stress (V_{stress}/V_{out}) on the components for the worst conditions during the three operation modes*

Fig. 8 depicts diagram of the designed controller system for the operation modes. At the first step, input current, input voltage, output current and output voltage have to be sampled using feedbacks and current sensors. The next part is mode diagnosis unit, which distinguishes operation mode of the converter by comparing input power and output power. Furthermore, condition of the battery is important in definition of the modes. As an example, when $P_{out} \leq P_{in}$ and $V_b < V_{bmax}$, input source supplies the load and charges the battery that is defined with charging mode. The other parts of the diagnosis unit are arranged based on descriptions in the previous sections. Last part of the diagram contains designed compensators for each mode that are activated depending on the diagnosed modes. Consequence of the controller diagram is PWM signals with calculated duty cycles to regulate output voltage and input power. The diagram provides continuous control of the converter during variation of the conditions. The diagnosis unit switches appropriate compensators to the control loop that is key of the continuously.

5 Selection and design of the components

To prepare a prototype for the proposed converter, its components are designed based on the worst conditions in the modes. The following steps illustrate procedure of choosing the components.

- *Selection of semiconductors*: main parameters of choosing a power switch for DC–DC converters are maximum voltage stress on them and peak of current flowing in them. According to Fig. 2, voltage stress on S_1, S_2 and S_3 as per the three modes are equal to V_o, V_b, and V_b, respectively. In the experiments, a 12 V battery is used and output voltage is regulated on 120 V. Thus, IRFP260N and IRFZ44N are chosen for S_1, S_2 and S_3. IRFP260N withstands reverse voltage until 200 V and its nominal current is high that makes it a suitable candidate to be

used as S_1. In addition, IRFZ44N withstands reverse voltage until 55 V and it is suitable to be used as S_2 and S_3. Furthermore, the two used MOSFETs have low r_{DS} that causes the converter performance with higher efficiency.

Similar to the power switches, the diodes are chosen based on the maximum reverse voltage per the three modes. According to the analysis, maximum voltage stress on D_3, D_4 and D_5 are V_o, V_b and V_b, respectively. The diodes D_1 and D_2 should withstand voltage from V_{in} until V_o. Therefore, MBR10100CT is chosen to be used as D_3 and D_4 that withstands voltage stress until 100 V. For D_1, D_2 and D_3, a diode with higher nominal voltage has to be chosen. So, MBR10200CT with 200 V nominal voltage is used for the diodes. Fig. 9 illustrates voltage stress on the components for the worst conditions. The curves are extracted from the analysis in the three modes. Input voltage and output voltage in the experiments are 25 V and 120 V, respectively that show voltage gain is five approximately. Utilising data of Fig. 9 for voltage gain equal to five demonstrates appropriate selection of the semiconductors. In addition, the used semiconductors can withstand the highest voltage stress in the other voltage gains.

- *Design of the capacitors*: the capacitors have to be designed based on voltage ripple and voltage stress on them. Voltage stress on C_1 and C_2 can be concluded from Fig. 9 for the defined voltage gain. Their capacitance should be determined using the operation modes analysis as follows:

According to Fig. 2*a*, current equation of C_2 is written as below:

$$C_2 \frac{\mathrm{d}V_{C2}}{\mathrm{d}t} = i_{C2on} \qquad (34)$$

Current of C_2 is equal to output current ($i_{C2on} = i_o$). If it has been assumed $\mathrm{d}t = 1/T_s$, $dV_{C2} = \Delta V_{C2} = \Delta V_O$ and $f_s = 1/T_s$, voltage ripple of C_2 is

$$\frac{\Delta V_{C2}}{V_{C2}} = \frac{\Delta V_o}{V_o} = \frac{d_1}{RC_2 f_s} \qquad (35)$$

Thus, capacitance of C_2 can be determined for a definite value of voltage ripple as below

$$C_2 \geq \frac{d_1}{R(\Delta V_{C2}/V_{C2})f_s} \qquad (36)$$

Using Fig. 2*a*, voltage ripple and capacitance of C_1 during the first mode are

$$\frac{\Delta V_{C_1}}{V_{C_1}} = \frac{d_1}{(1 - d_1)^2 R C_1 f_s} \tag{37}$$

$$C_1 \geq \frac{d_1}{(1 - d_1)^2 R (\Delta V_{C_1}/V_{C_1}) f_s} \tag{38}$$

The capacitors equations for the second and the third operation modes are obtained. The equations for the two modes are similar to each other, which are shown by (39) and (40).

$$C_1 \geq \frac{(d_1 + d_2)}{(1 - (d_1 + d_2))^2 R (\Delta V_{C_1}/V_{C_1}) f_s} \tag{39}$$

$$C_2 \geq \frac{(d_1 + d_2)}{R (\Delta V_{C_2}/V_{C_2}) f_s} \tag{40}$$

Using (36), (38)–(40), the capacitances are calculated for the worst conditions in the experiments. The values of f_s, R, $(d_1 + d_2)$, $\Delta V_{C_1}/V_{C_1}$ and $\Delta V_{C_2}/V_{C_2}$ are 25 kHz, 200 Ω, 0.7, 0.01 and 0.001, respectively. The minimum capacitances of C_1 and C_2 are calculated as follows:

$$C_1 \geq \frac{0.7}{(1 - 0.7)^2 200(0.01)25 \times 10^3} \rightarrow C_1 \geq 155\,\mu\text{F}$$

$$C_2 \geq \frac{0.7}{200(0.01)25 \times 10^3} \rightarrow C_1 \geq 140\,\mu\text{F}$$

The capacitor of C_2 is parallel with load that reduces the output voltage ripple. Thus, percentage of voltage ripple for C_2 is selected lower than C_1. Referring to the calculations, the capacitors should have capacitances higher than 155.5 μF and 140 μF. Therefore, two 220 μF capacitors are chosen for the prototype. Furthermore, their nominal voltages are considered in the selection that has to be higher than voltage stress of the worst conditions in Fig. 9.

- *Design of the inductors*: minimum inductance of the second inductor and current ripple of the first inductor are the two used methods to design them. The first inductor (L_1) is set for current ripple equal to average current in the worst condition. The method for L_1 is utilised because of its series connection with the input source. Lower current ripple of input source is important in quality of the converter performance.

According to Fig. 2a, the following equations for L_1 are written:

$$L\frac{\mathrm{d}i_{L_1}}{\mathrm{d}t} = V_{L_1} \text{ and } V_{L_1} = V_{\text{in}} \tag{41}$$

Assuming $\mathrm{d}t = d_1 T_s$, $\mathrm{d}i_{L_1} = \Delta I_{L_1}$, $f_s = 1/T_s$ and using (5) the below equation is obtained

$$L_1 = \frac{V_o (1 - d_1)^2}{\Delta I_{L_1} f_s} d_1 \tag{42}$$

Average current of the inductor is

$$I_{L_1} = \frac{V_o}{R(1 - d_1)^2} \tag{43}$$

Substituting (43) in (42), the inductance equation for a certain current ripple is:

$$L_1 = \frac{R(1 - d_1)^4 d_1}{(\Delta I_{L_1}/I_{L_1}) f_s} \tag{44}$$

The second inductor is designed based on minimum inductance and common boundary condition that considers $I_{L\text{min}} = 0$ ($I_{L_2} = \Delta I_{L_2}/2$). Referring to Fig. 2a, V_{L_2} is equal to V_{C_1}, thus, (45) is written.

$$\Delta I_{L_2} = \frac{d_1 T_s V_{C_1}}{L_2} \tag{45}$$

Using the boundary condition and substituting (2) and (5) into (45), minimum inductance of L_2 is obtained as below

$$L_{2\text{min}} = \frac{d_1 (1 - d_1)^2 R}{2 f_s} \tag{46}$$

According to (44) and (46), maximum values of L_1 and L_2 for the worst conditions have to be determined per d_1 equal to 0.2 and 1/3, respectively. Thus, the inductors are calculated for $R = 200\ \Omega$ and $f_s = 25$ kHz

$$L_1 = \frac{200(1 - 0.2)^4 \times 0.2}{1 \times 25 \times 10^3} = 655.36\,\mu\text{H}$$

$$L_{2\text{min}} = \frac{200(1 - (1/3))^4 \times (1/3)}{2 \times 25 \times 10^3} = 593\,\mu\text{H}$$

In the second operation mode, the input source supplies the load and the battery that may cause increasing current ripple. To prevent higher current ripple and discontinuous conduction mode, the inductances are assumed to be 10–20% bigger. Thus, L_1 and L_2 for the prototype are chosen to be 700 μH.

6 Experimental results

In order to verify the proposed converter operation, a prototype is prepared as depicted in Fig. 10a.

The prototype is implemented for 90 W output power. In the experiments, an input source with constant voltage equal to 25 V is utilised instead of the renewable source. Furthermore, a 12 V lead-acid battery is connected to the proposed bidirectional path (V_b in Fig. 10 is the input port for the battery). The control board consists of drivers and a Texas Instrument DSP. Table 3 shows details of the used components in the prototype.

The proposed converter is tested in the three operation modes by regulating the input current references, which simulates the


a

b
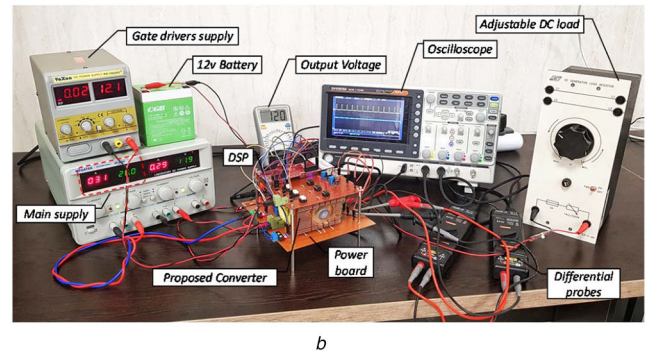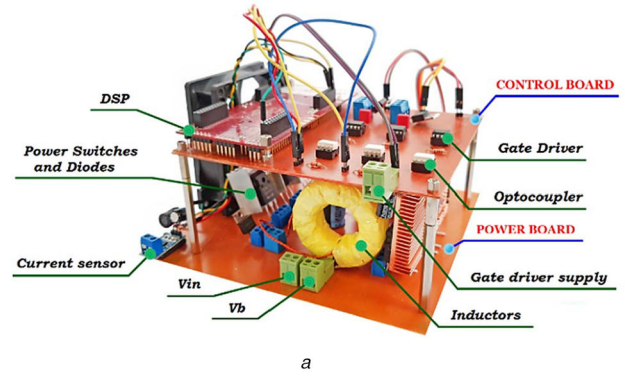
Fig. 10 *Prototypes and experimental arrangements*
(a) Prototype of the proposed converter and control board,
(b) Experimental bench and arrangements of used components

Table 3 Utilised components in the prototype and their details

	Mosfets		Diodes		Capacitors	Inductors
	$S1$	$S2, S3$	$D1, D2, D3$	$D4, D5$	$C1, C2$	$L1, L2$
type parameters	IRFP260N	IRFZ44N	MBR30200PT	MBR10100CT	Taicon	700 μH
	$r_{DS} = 0.04\ \Omega$	$r_{DS} = 0.03\ \Omega$	$t_{rr} \simeq 100$ nS	$t_{rr} \simeq 100$ nS	220 μF	
	$V_{DS} = 200$ V	$V_{DS} = 55$ V	$V_F = 0.8$ V	$V_F = 0.6$ V	200 V	
	$I_D = 50$ A	$I_D = 49$ A	$V_{AK} = 200$ V	$V_{AK} = 100$ V	$r_C = 0.01\ \Omega$	
other properties		$R_o = (200–240)\Omega$		$f_s = 25$ kHz, $V_{in} = 25$ V, $V_b = 12$ V		
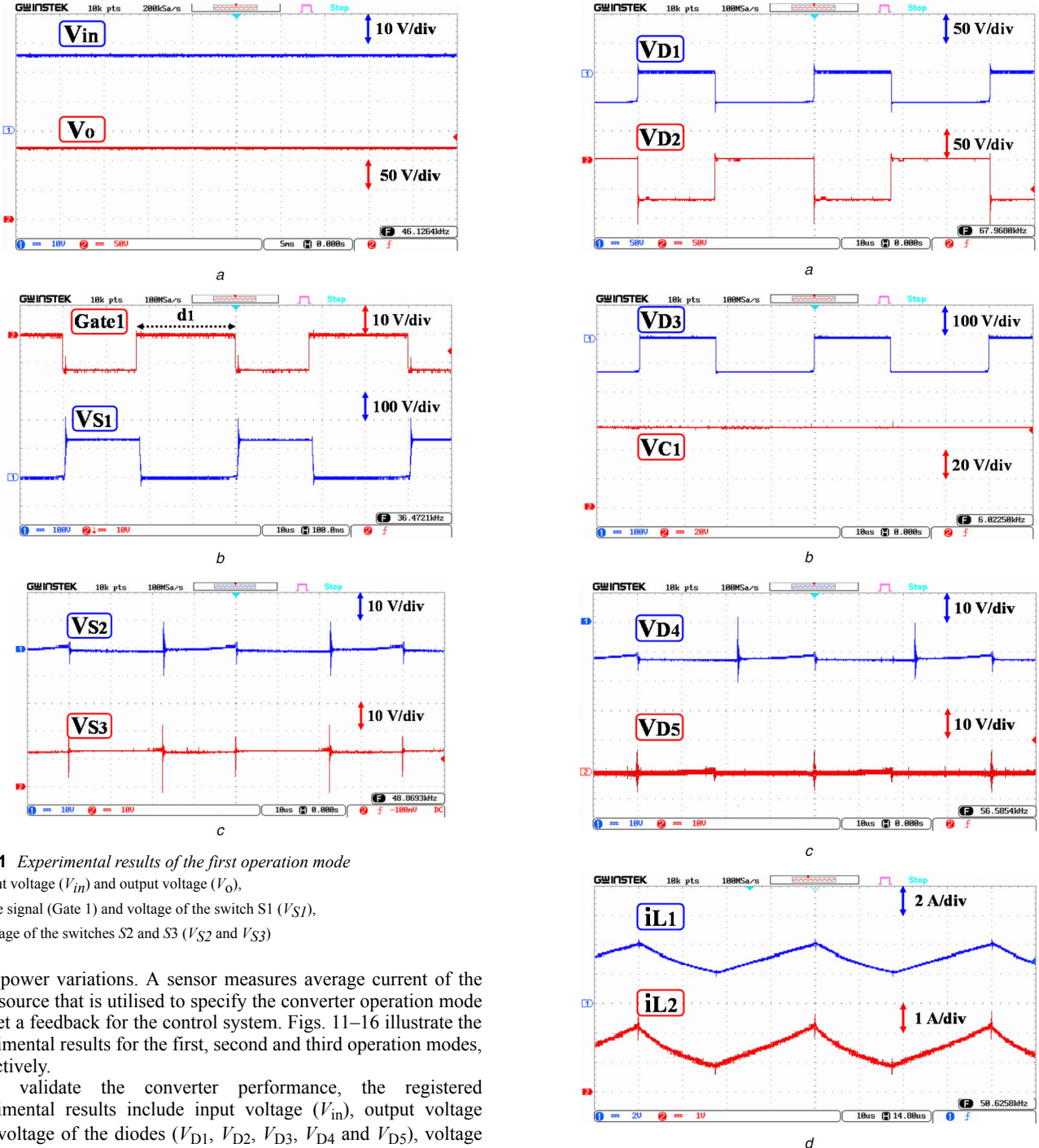
Fig. 11 *Experimental results of the first operation mode*
(a) Input voltage (V_{in}) and output voltage (V_o),
(b) Gate signal (Gate 1) and voltage of the switch S1 (V_{S1}),
(c) Voltage of the switches $S2$ and $S3$ (V_{S2} and V_{S3})

Fig. 12 *Experimental results of the first operation mode*
(a) Voltage of the diodes $D1$ and $D2$ (V_{D1} and V_{D2}),
(b) Voltage of the diode $D3$ (V_{D3}) and voltage of the capacitor $C1$ (V_{C1}),
(c) Voltage of the diodes $D4$ and $D5$ (V_{D4} and V_{D5}), *(d)* The inductors current (i_{L1} and i_{L2})
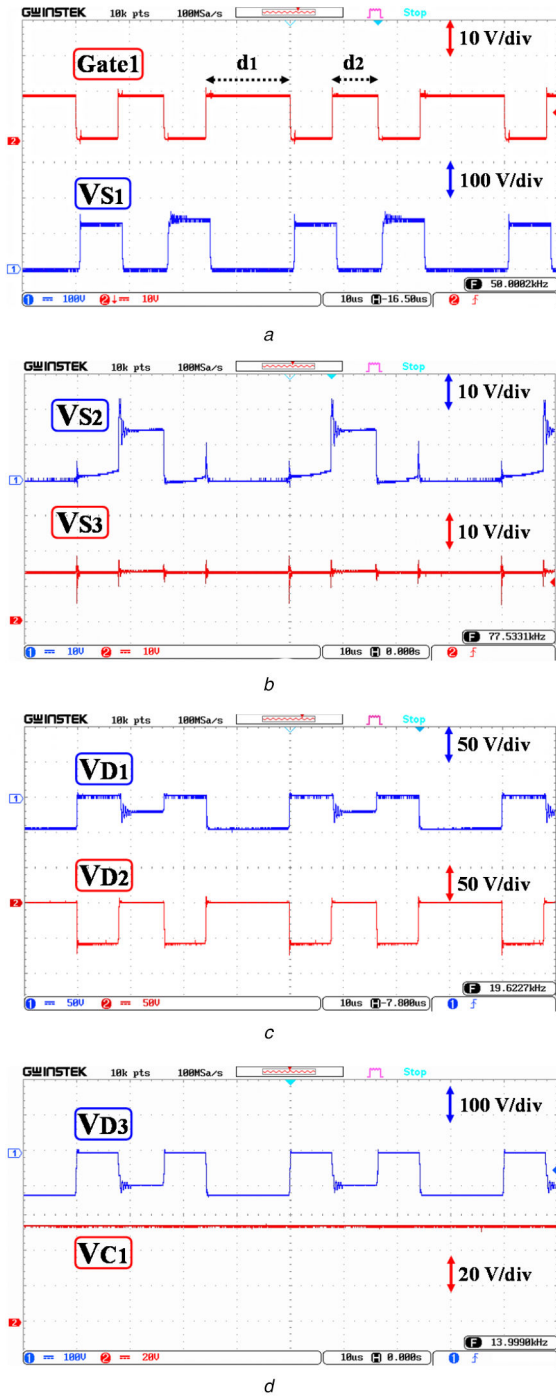
input power variations. A sensor measures average current of the input source that is utilised to specify the converter operation mode and get a feedback for the control system. Figs. 11–16 illustrate the experimental results for the first, second and third operation modes, respectively.

To validate the converter performance, the registered experimental results include input voltage (V_{in}), output voltage (V_o), voltage of the diodes (V_{D1}, V_{D2}, V_{D3}, V_{D4} and V_{D5}), voltage of the switches (V_{S1}, V_{S2} and V_{S3}), the battery current (i_b), the battery voltage (V_b) and the inductors current (i_{L1} and i_{L2}).

In the first operation mode, the control system regulates output voltage and there is no need to control input current. The load resistance is 200 Ω and output voltage reference is set to 120 V. Thus, the proposed converter supplies a 72 W output power. In the first state of the mode, D_1, D_5, S_1 and S_2 are conducting (Figs. 11 and 12). The second state of the mode includes conduction of D_1

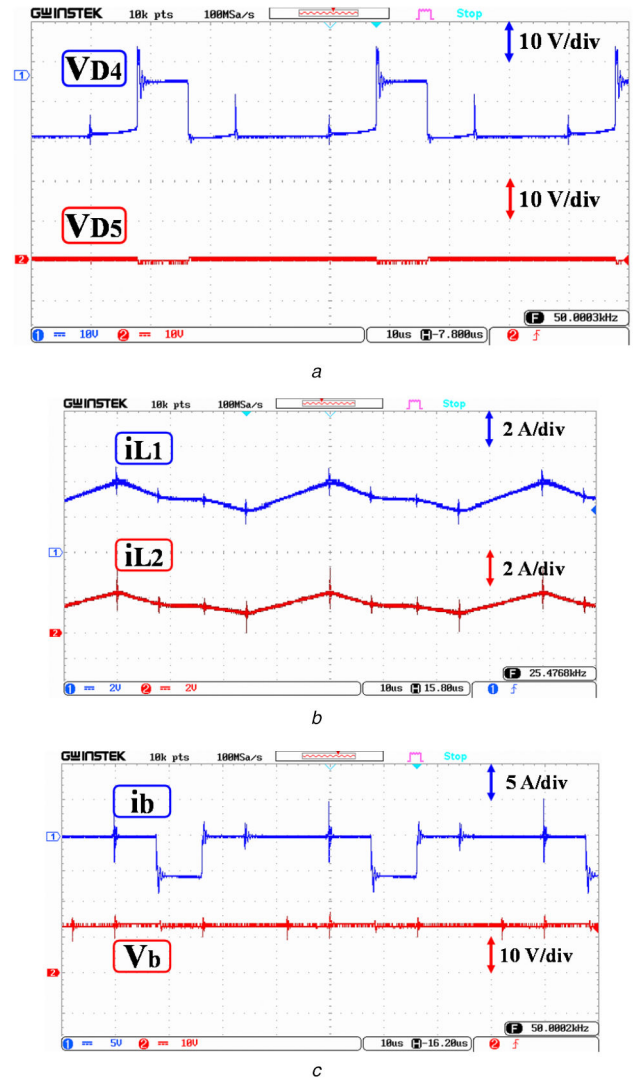**Fig. 13** *Experimental results of the second operation mode (charging mode)*

(a) Gate signal (Gate 1) and voltage of the switch $S1$ (V_{S1}),

(b) Voltage of the switches $S2$ and $S3$ (V_{S2} and V_{S3}),

(c) Voltage of the diodes $D1$ and $D2$ (V_{D1} and V_{D2}),

(d) Voltage of the diode $D3$ (V_{D3}) and voltage of the capacitor $C1$ (V_{C1})

and D_3. The input current is continues with average equal to 3.04 A (i_{L1}).

The second operation mode is tested with current reference equal to 3.5 A and the converter charges the battery. The first and second states of the mode are as same as the first mode in which the converter transfers power to the load with duty cycle equal to d_1. The semiconductors operate similar to the previous mode (Figs. 11 and 12) and the switches S_1 and S_2 are turned on by PWM signal. The third switching state includes battery-charging mode with battery current and its average equal to 5.8 A and 1.22 A, respectively. In this state, the duty cycle is considered on the gate signal as d_2 (Fig. 13). Furthermore, discharging of the inductors are
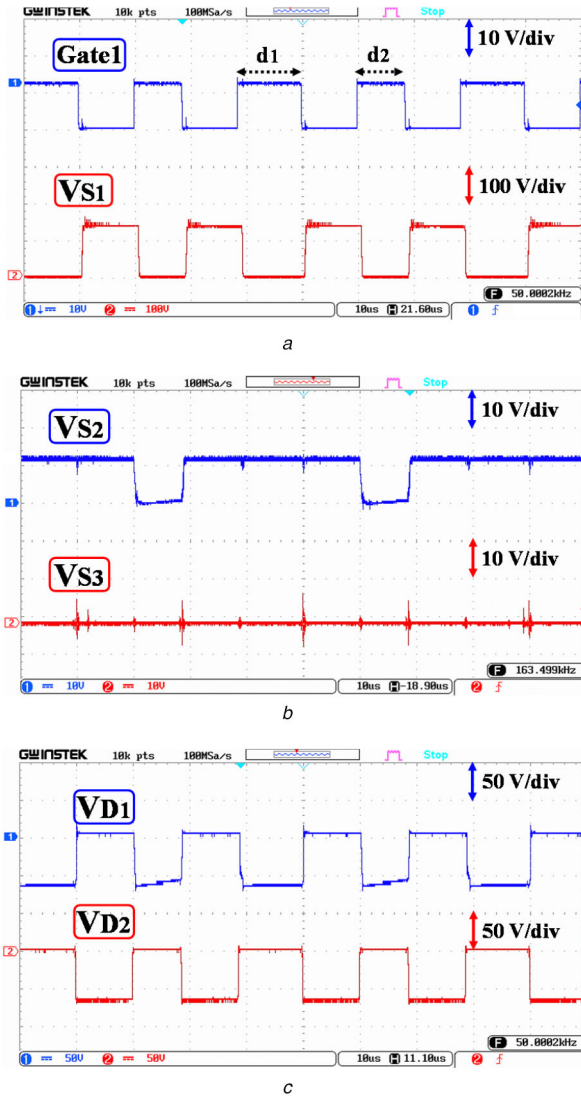

Fig. 14 *Experimental results of the second operation mode (charging mode)*

(a) Voltage of the diodes $D4$ and $D5$ (V_{D4} and V_{D5}),

(b) The inductors current (i_{L1} and i_{L2}),

(c) The battery current (i_b) and the battery voltage (V_b)

stopped and they are charging with low slopes. This reduces discharging periods of the inductors and their current ripples (it can be concluded from comparing the inductors current in Figs. 12 and 14). The fourth-switching state of the mode is the same as the second switching state and the inductors are discharged to supply the load current. In the experiment d_1 and d_2 are equal to 0.39 and 0.21, respectively. The converter supplies the load (220 Ω–65.45 W) and the battery (14.6 W) during the second mode with input power equal to 87.5 W.

The third operation mode is tested with current reference equal to 2.5 A. The battery is discharged to take part in supplying the load. The first and second states of the mode are as same as the first operation mode in which the converter transfers power to load with duty cycle equal to d_1. The semiconductors operate similar to the previous mode and the switches S_1 and S_2 are turned on by PWM signal. The third switching state includes battery-discharging mode with battery current equal to 5.38 A (the battery average current per a cycle is 1.18 A). The discharging path is prepared by the three switches S_1, S_2 and S_3, which are turned on simultaneously (Fig. 15). In the state, duty cycle is considered on the gate signal as d_2 (Fig. 15). Furthermore, discharging of the inductors is stopped and they are charged. This reduces discharging time of the inductors and their current ripples (compare Fig. 12 and Fig. 16). The forth-switching state of the mode is as same as the second switching state and the inductors are discharged to supply
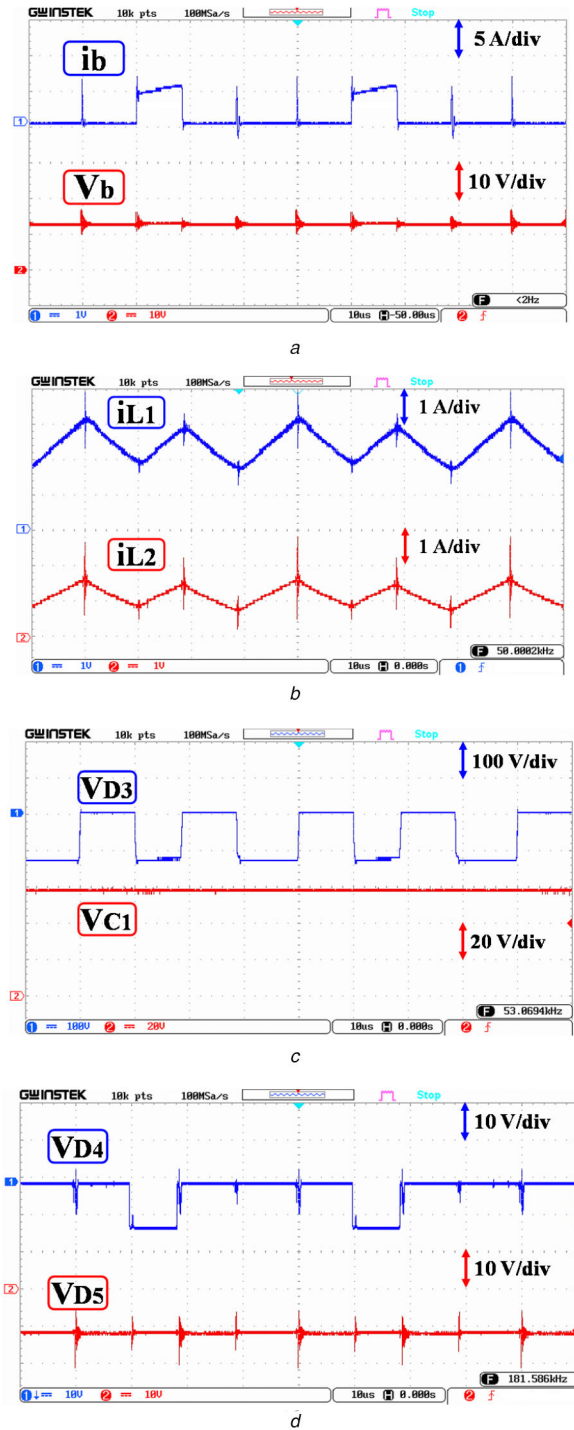
Fig. 15 *Experimental results of the third operation mode (discharging mode)*

(a) Gate signal (Gate 1) and voltage of the switch $S1$ (V_{S1}),

(b) Voltage of the switches $S2$ and $S3$ (V_{S2} and V_{S3}),

(c) Voltage of the diodes $D1$ and $D2$ (V_{D1} and V_{D2})

the load. In the experiment, d_1 and d_2 are equal to 0.285 and 0.22, respectively. During third operation mode, the converter supports 72 W (200 Ω) output power with 14.2 and 62.5 W form the battery and input source, respectively.

In order to verify the converter dynamic and effectiveness of the designed control system, variation of the three modes in short time is examined (Fig. 17). The battery current is varied based on the system condition and this occurs very fast by the control system. The time of the voltage regulation shows that the modes are changed in short times (Fig. 17). The test is done in several conditions that demonstrate good dynamic of the converter, high speed of the control system and stability of the system.

The converter efficiency during load variation ($P_o \leq 100\,\text{W}$) is extracted from the experiments. The experiment results consist of the three operation modes, which are depicted in Fig. 18. As shown in Fig. 18, the efficiency curves from up to down are the first operation mode (quadratic), the third operation mode (discharging) and the second operation mode (charging), respectively. The converter operates with efficiency equal to 93% in the first operation mode for $P_o \leq 100\,\text{W}$. The results demonstrate efficiency >90% for $P_o \leq 100\,\text{W}$ in the third operation mode and for $P_o \leq 70\,\text{W}$ in the second operation mode (Fig. 18). The converter efficiency in a definite output power can be considered with an average of the three modes efficiencies. According to the results,


Fig. 16 *Experimental results of the third operation mode (discharging mode)*

(a) The battery current (i_b) and the battery voltage (V_b),

(b) The inductors current (i_{L1} and i_{L2}),

(c) Voltage of the diode $D3$ (V_{D3}) and voltage of the capacitor $C1$ (V_{C1}),

(d) Voltage of the diodes $D4$ and $D5$ (V_{D4} and V_{D5})

the average efficiency of the converter for $P_o = 70\,\text{W}$ and $P_o = 90$ W is equal to 93 and 91%, respectively. Since the TPC converter is designed for $P_o = 90\,\text{W}$, the results confirmed the high efficiency performance.

7 Conclusion

The proposed converter is an integration of a quadratic boost DC–DC converter with an ES system to apply in case of a stand-alone PV systems. The proposed battery connection in charging/discharging modes has a simple structure, which is made of two
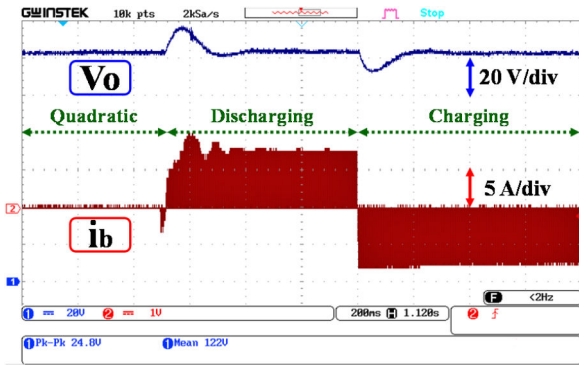
Fig. 17 *Control of the proposed converter during the operation mode variations – the battery current (i_b) and output voltage (V_O) are shown in the experiment*
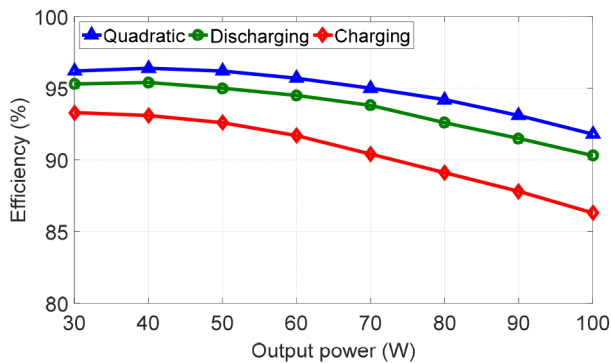
Fig. 18 *Proposed converter efficiency during load variation for the three operation modes – first mode: quadratic, second mode: charging and third mode: discharging*

diodes and three switches (including the converter power switch). The main advantages of the converter are its simple structure with high voltage gain. Furthermore, the converter operation modes are regulated in single stages that reduce power losses and increase efficiency. According to the experimental results, the proposed converter and the control system meet the requirements with qualified performance.

The proposed converter is compared with the similar converters. As the main results of the comparisons, the proposed converter includes positive points from view of the main quality factors. The positive points can be considered by its higher voltage gain, acceptable number of the used components, continuously of input current, existence of a bidirectional path, existence of a common ground and high efficiency of its performance. It is worthy to say, none of the compared converters have the advantages at the same time and each of them has one or two drawbacks in comparison to the proposed one. Thus, the proposed converter can be presented as a high voltage gain converter with noticeable positive points for PV/battery systems.

8 Acknowledgment

9 References

[1] Banaei, M.R., Ardi, H., Alizadeh, R., *et al.*: 'Non-isolated multi-input–single-output DC/DC converter for photovoltaic power generation systems', *IET Power Electron.*, 2014, **7**, (11), pp. 2806–2816
[2] Kim, T., Kwak, S.: 'Single pole switch leg based multi-port converter with an energy storage', *IET Power Electron.*, 2016, **9**, (6), pp. 1322–1330
[3] Zhang, N., Sutanto, D., Muttaqi, K.M.: 'A review of topologies of three-port DC–DC converters for the integration of renewable energy and energy storage system', *Renew. Sust. Energy Rev.*, 2016, **56**, pp. 388–401
[4] Kumar Bhattacharjee, A., Kutkut, N., Batarseh, I.: 'Review of multiport converters for solar and energy storage integration', *IEEE Trans. Power Electron.*, 2019, **34**, (2), pp. 1431–1445
[5] Wu, H., Zhang, J., Xing, Y.: 'A family of multiport buck–boost converters based on DC-link-inductors (DLIs)', *IEEE Trans. Power Electron.*, 2014, **30**, (2), pp. 735–746
[6] Zhang, P., Chen, Y., Kang, Y.: 'Non-isolated wide operation range three-port converters with variable structures', *IEEE J. Emerg. Sel. Top. Power Electron.*, 2017, **5**, (2), pp. 854–869
[7] Prabhala, V.A.K., Fajri, P., Gouribhatla, V.S.P., *et al.*: 'A DC-DC converter with high voltage gain and two input boost stages', *IEEE Trans. Power Electron.*, 2015, **31**, (6), pp. 4206–4215
[8] Deihimi, A., Mahmoodieh, M.E.S.: 'Analysis and control of battery-integrated dc/dc converters for renewable energy applications', *IET Power Electron.*, 2017, **10**, (14), pp. 1819–1831
[9] Zhu, H., Zhang, D., Zhang, B., *et al.*: 'A non-isolated three-port DC-DC converter and three domain control method for PV-battery power systems', *IEEE Trans. Ind. Electron.*, 2015, **62**, (8), pp. 4937–4947
[10] Wu, H., Sun, K., Ding, S., *et al.*: 'Topology derivation of nonisolated three-port DC–DC converters from DIC and DOC', *IEEE Trans. Power Electron.*, 2012, **28**, (7), pp. 3297–3307
[11] Cheng, T., Lu, D.D., Qin, L.: 'Non-isolated single-inductor DC/DC converter with fully reconfigurable structure for renewable energy applications', *IEEE Trans. Circuits Syst.*, 2017, **65**, (3), pp. 351–355
[12] Haghighian, K., Tohidi, S., Feyzi, M.R., *et al.*: 'Design and analysis of a novel SEPIC-based multi-input DC/DC converter', *IET Power Electron.*, 2017, **10**, (12), pp. 1393–1402
[13] Faraji, R., Farzanehfard, H.: 'Soft-switched non-isolated high step-up three-port DC-DC converter for hybrid energy systems', *IEEE Trans. Power Electron.*, 2018, **33**, (12), pp. 10101–10111
[14] Boora, A.A., Zare, F., Ghosh, A.: 'Multi-output buck–boost converter with enhanced dynamic response to load and input voltage changes', *IET Power Electron.*, 2011, **4**, (2), pp. 194–208
[15] Babaei, E., Abbasi, O.: 'Structure for multi-input multi-output dc–dc boost converter', *IET Power Electron.*, 2016, **9**, (1), pp. 9–19
[16] Chen, Y., Huang, A.Q., Yu, X.: 'A high step-up three-port DC-DC converter for stand-alone PV/battery power systems', *IEEE Trans. Power Electron.*, 2013, **28**, (11), pp. 5049–5062
[17] Chien, L.J., Chen, C.C., Chen, J., *et al.*: 'Novel three-port converter with high-voltage gain', *IEEE Trans. Power Electron.*, 2013, **29**, (9), pp. 4693–4703
[18] Behjati, H., Davoudi, A.: 'Single-stage multi-port DC–DC converter topology', *IET Power Electron.*, 2013, **6**, (2), pp. 392–403
[19] Nejabatkhah, F., Danyali, S., Hosseini, S.H., *et al.*: 'Modeling and control of a new three-input DC–DC boost converter for hybrid PV/FC/battery power system', *IEEE Trans. Power Electron.*, 2011, **27**, (5), pp. 2309–2324
[20] Nahavandi, A., Hagh, M.T., Sharifian, M.B.B., *et al.*: 'A non-isolated multi-output DC–DC boost converter for electric vehicle applications', *IEEE Trans. Power Electron.*, 2014, **30**, (4), pp. 1818–1835
[21] Uno, M., Sugiyama, K.: 'Switched capacitor converter based multiport converter integrating bidirectional PWM and series-resonant converters for standalone photovoltaic systems', *IEEE Trans. Power Electron.*, 2018, **34**, (2), pp. 1394–1406
[22] Varesi, K., Hosseini, S.H., Sabahi, M., *et al.*: 'Modular non-isolated multi-input high step-up dc–dc converter with reduced normalized voltage stress and component count', *IET Power Electron.*, 2018, **11**, (6), pp. 1092–1100
[23] Qian, Z., Rahman, O.A., Atrash, H.A., *et al.*: 'Modeling and control of three-port DC/DC converter interface for satellite applications', *IEEE Trans. Power Electron.*, 2009, **25**, (3), pp. 637–649
[24] McDonough, M.: 'Integration of inductively coupled power transfer and hybrid energy storage system: a multi-port power electronics interface for battery powered electric vehicles', *IEEE Trans. Power Electron.*, 2015, **30**, (11), pp. 6423–6433
[25] Ahrabi, R., Ardi, H., Elmi, M., *et al.*: 'A novel step-up multiinput DC–DC converter for hybrid electric vehicles application', *IEEE Trans. Power Electron.*, 2016, **32**, (5), pp. 3549–3561